Infrared diffuse reflectance instrumentation and standards at NIST

Leonard M. Hanssen[*], Simon Kaplan

Optical Technology Division, NIST, Gaithersburg, MD 20899, USA

Abstract

A spectrophotometer system for spectral characterization of materials in the infrared has been built around a bench-top Fourier transform instrument. Its capabilities include the measurement of directional-hemispherical reflectance from 1 to 18 µm. The spectral reflectance measurement is performed with an integrating sphere with an incidence angle of $8°$. Both relative and absolute measurements can be made. Several methods can be used to determine the absolute value of the directional-hemispherical reflectance of samples. The primary method used is independent of the integrating sphere theory and the requisite assumptions associated with its use. The calibration of a standard reference material (SRM) is described. This SRM has a reflectance value near 0.9 over the complete calibration range 2–18 µm. As part of the calibration procedure the spatial uniformity of the sphere throughput and the bi-directional reflectance distribution function (BRDF) of the SRM material are evaluated. © 1999 Published by Elsevier Science B.V. All rights reserved.

Keywords: Infrared; Spectral reflectance; Directional-hemispherical reflectance; Diffuse reflectance; Integrating sphere

1. Introduction

Over the past years, the Optical Technology Division at the National Institute of Standards and Technology has been developing a facility for the spectral characterization of the optical properties of materials in the infrared to complement parallel developments in infrared detector and source characterization and calibration [1–3]. An important characterization capability is that of the spectral reflectance (and transmittance) of materials which scatter light in a non-specular fashion, whether due to surface or volume effects. The spectral absorptance and emittance can also be indirectly obtained from the reflectance measurement (for opaque samples) and additionally the transmittance measurement (for translucent samples). The NIST program of instrumentation development for directional-hemispherical reflectance (DHR)[1] has been described in an earlier paper [4]. Both an integrating sphere system as well as a hemi-ellipsoidal collecting mirror system were constructed for absolute DHR measurement. Based on an overall performance comparison of the two systems and the limited

---

*Corresponding author. Tel.: +1-301-975-2334; fax: +1-301-840-8551; e-mail: hanssen@nist.gov

[1]We shall refer to directional-hemispherical reflectance in this paper. However, the results and discussion apply equally to hemispherical-directional reflectance (HDR) via reciprocity, and to 'diffuse reflectance' as well.

resources available, the integrating sphere system was selected for the initial development of DHR measurement capability.

The history of the integrating spheres for DHR measurement in the infrared spectral region beyond 5 µm is relatively recent, beginning with the development of the first rough-gold-coated integrating sphere in 1976 [5]. Since that time, the importance of accurate diffuse reflectance measurements has grown along with the number of instruments in use. Unfortunately, it is not clear that the measurement accuracy of the available instrumentation has proceeded apace. Support of the user community by the development of standards and calibration facilities at the primary national standards laboratories is critical to the realization of the full potential of the reflectance instrumentation.

In this paper we describe the integrating sphere system in Section 2, sources of measurement error and their evaluation in Section 3, the methodology for the determination of the absolute DHR in Section 4, the application of the method to the characterization of an infrared DHR standard in Section 5, and a discussion of the results in Section 6.

2. Instrumentation and measurement method

A description of the original integrating sphere design considerations is given in [4]. Critical design issues include the selection of a coating and arrangement of the ports, baffles, detector and its field-of-view (FOV). The best generally available integrating sphere coatings for the infrared deviate significantly from the ideal Lambertian scatterer [4]. Monte Carlo integrating sphere simulation studies have shown that this can lead to significant measurement error, even for an otherwise well-designed sphere [6]. Many sphere designs, especially ones used for absolute measurement, are based on the integrating sphere theory that assumes not only an ideal behavior of the sphere coating, but also an ideal sphere geometry. By ideal sphere geometry, we mean that: (a) all reflecting surfaces in the sphere lie exactly on the geometrical sphere surface; (b) no light which exits an empty port returns back into the sphere; and (c) baffles do not exist. All spheres (some more than others) tend to

deviate from these ideal attributes, which may result in measurement errors. The NIST integrating sphere has been designed with several features to enable it to be configured close to an ideal sphere: (a) port covers curved to match the sphere surface and coated in the same way as the main sphere; (b) knife-edge ports with complete clearance for light to leave the sphere without striking any mounting hardware; and (c) removable baffles. These features allow one to perform a series of measurements (detailed in [4]) to obtain the absolute DHR. Based on results of the sphere characterization described below, however, a different approach has been developed.

The integrating sphere design schematic is shown in Fig. 1 (the sphere has undergone some modifications from the design presented in [4]). The sphere has an inner diameter of 152 mm. A focused input beam from the FTIR is incident on the sample or reference as the sphere is rotated between two positions indicated by the two input beam arrows in Fig. 1(b). The two positions are used in a relative reflectance measurement. The angle of incidence is $8°$. This angle was selected to be near normal, and yet prevent retro-reflection (and hence entrance port loss) of any portion of an *f*/5 focused incident beam on a specular sample. The original design included a rotation stage, whose axis of rotation was centered on the sphere entrance port. In the present design, to enable greater versatility in measurement, the single rotation stage has been replaced by two rotation stages: one stage with its rotation axis centered on the sphere central axis (the center of Fig. 1(b)), mounted on a second stage whose axis of rotation is centered at the beam focus at the sphere wall (such as the sample position in Fig. 1(b)). The double rotation stage system is used to allow both reflectance and transmittance measurements in an absolute way. Also, three baffles are shown which shade the sample, reference, and the detector from each other and the detector FOV from the sample and reference. The detector is a liquid N_2 cooled Hg:Cd:Te (MCT) detector with a non-imaging concentrator built into its dewar for maximization of throughput and optimization of the FOV. By 'throughput' we mean the efficiency of transferring flux from one point to another (e.g. from the sphere to the detector). The details of the detector/concentrator design are described in [7]. The sphere coating is a plasma sprayed metal, over-coated with electroplated gold,
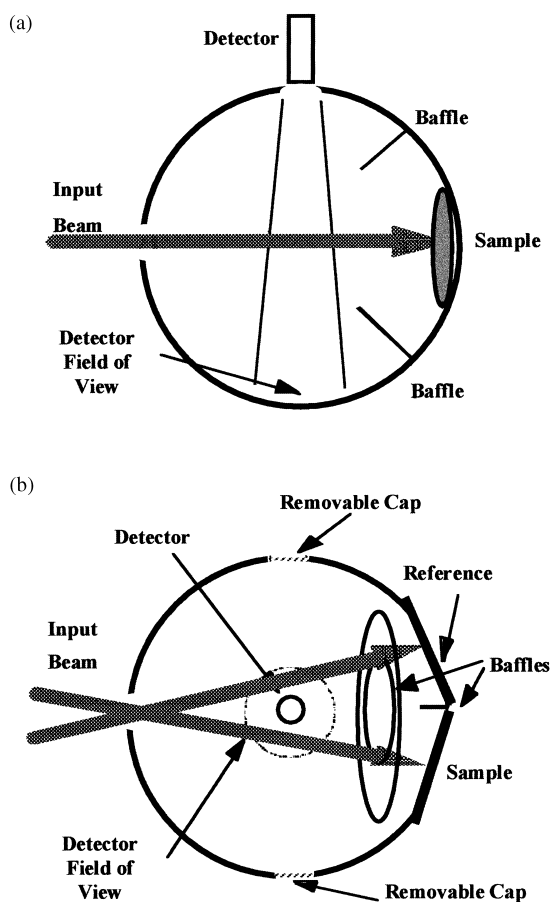
(a)

(b)

Fig. 1. Schematic of integrating sphere layout showing side (a) and top (b) views. Three baffles are shown which shade the sample, reference and detector from each other and the detector FOV from the sample and reference. The sphere position can be rotated to allow the beam to be incident anywhere along the central circle of the sphere and specifically on the sample and reference. These two arrangements are used for a relative reflectance measurement. Removable caps are used as a means to measure the sphere wall reflectance [4].

a proprietary coating produced by Labsphere[2] [8], which also manufactured the integrating sphere to NIST specifications. The coating was selected because it is a very good infrared diffuser, as demonstrated in [4], as well as in Section 5.

---

[2] The mention of manufacturers and model names is intended solely for the purpose of technical information useful to the reader and in no way should be construed as an endorsement of the named manufacturer or product.

The integrating sphere receives its input light from an FTIR via interface optics as described in a companion paper [9]. The spectral range of the measurements are from 1 to 15 μm (10 000–600 cm^{-1}) and 1–18 μm (10 000–540 cm^{-1}) for the two MCT detectors. (Some figures are presented with a wave number scale for clarity or other requirements.) The FTIR is set up in two configurations: with a coated quartz beam splitter and a quartz envelope tungsten–halogen lamp for the near infrared (NIR) (1–3 μm) and with a coated KBr beam splitter and a heated SiC source for the mid-infrared (2–18 μm). The measurements were taken with constant resolutions of 4 or 8 cm^{-1}. The entire measurement system operates under a purge gas environment consisting of air from which H_2O and CO_2 (and their resultant infrared absorption lines) have been removed. The measurement geometry for all relative reflectance measurements with the sphere is shown in Fig. 1(b), where sample and reference measurements are performed sequentially with the beam incident on the sample and reference, respectively.

For all absolute reflectance measurements, the geometry is shown in Fig. 2. The reference measurement (Fig. 2(a)) is made with the input beam entering the sphere through the empty reference port and incident on the sphere wall adjacent to the primary entrance port. The region of incidence is the same as that which would be illuminated by the reflected beam off a specular reference in a relative reflectance measurement. The sample measurement is made in the conventional arrangement shown in Fig. 2(b). The specular component of the sample reflected light is incident on a region adjacent to the entrance port and symmetrically positioned with respect to the reference input shown in Fig. 2(a). This same geometry is used for the absolute reflectance measurements of specular samples [9,10]. For transmittance measurements, the beam is brought in from behind the sample. This is accomplished by a 180° rotation in Fig. 2(b) of the sphere about the sample port.

To enable transmittance measurements and accurate reflectance measurements on transmitting samples, the mounting hardware is designed to hold samples from the outside edges. In addition an 8° compensating wedge and mounts have been made to enable measurement of normal incidence transmittance and to separate the diffuse and specular components in
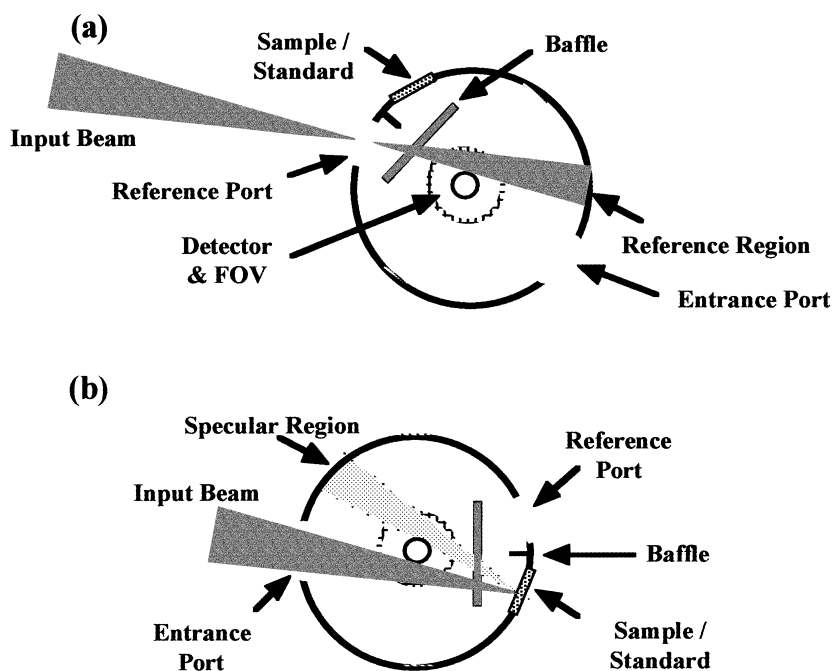
Fig. 2. Absolute reflectance measurement geometry showing (a) the reference measurement geometry and (b) the sample reflectance measurement geometry. The sample transmittance geometry (not shown) is a slight modification of (a), with the sphere slightly rotated about its center so that the beam is incident on the back of the sample. In this last case the transmitted light for a non-scattering material would be incident on the same specular region as shown in (b).

reflectance. For transmittance, the specular component can be removed without the aid of a wedge. This is accomplished by rotating the sphere to the position for $-8°$ incidence on the sample, for which the specularly transmitted beam will exit the sphere through the entrance port.

For specular samples, the ratio of a reflectance or transmittance measurement to a reference measurement, shown schematically in Fig. 2, is the absolute reflectance or transmittance, for equal throughput of the 'specular' and 'reference' regions in Fig. 2. Small differences in the throughput can be directly measured and corrected for [9,10].

For scattering samples, the reflected (or transmitted) light is spread out over the entire sphere and encounters a non-uniform throughput. The ratio of measurements would produce an accurate absolute result if the throughput were perfectly uniform. The uncertainty of the DHR result will then depend on the size of the non-uniformity and the extent to which it can be corrected for.

3. Integrating sphere characterization

3.1. Sources of error overview

To evaluate the accuracy of the sphere-based measurements, a number of potentially significant sources of error need to be examined. For the DHR measurements these fall into three categories: errors associated with

1. the spectrophotometer instrumentation and electronics;
2. the sphere, sample, and beam geometry and the interactions between them; and
3. the use of equations based on ideal sphere theory to calculate or correct for the absolute DHR of the samples.

For our primary absolute method described in Section 4, the third category is not a significant factor. That is because the method does not make any

assumptions about the characteristics of the sphere coating or the sphere behavior; it does not rely upon the integrating sphere theory.

The first category is perhaps the most significant one, in terms of the largest potential contribution to the total error or measurement uncertainty. Under a wide variety of circumstances, if not carefully evaluated, FTIR measurements can easily lead to large errors. However, we are addressing many of the major sources of error in FTIR measurements [11,12], and use multiple methods and intercomparisons [11], whenever possible, to assess the true size of errors and uncertainties in the measurements. A good illustration is the use of the integrating sphere described in this paper for specular reflectance and transmittance measurements, which is described in detail in [9]. The resulting levels of relative expanded uncertainty due to FTIR error sources have been reduced to ~0.5% or lower under most circumstances [9]. This level of uncertainty does not contribute significantly to the expanded (total) uncertainty.

This leaves us with the second category to consider. For each specific error source, the size of the error will depend on the sample and its characteristics. Many of the error sources have been evaluated and the resulting uncertainties are less than or equal to 0.001 (absolute). These include: (a) inter-reflections between sample, detector and the interferometer; (b) emission from sample and detector, and its modulation by the FTIR; (c) beam overfilling the entrance port in the sample reflectance measurement; (d) beam overfilling the sample (or reference) port in the reflectance measurement; (e) alignment of the rotation stages, integrating sphere, and detector; (f) difference in sphere throughput between light leaving the sample and light leaving the reference.

The results of a test of error source (d) is shown in Fig. 3. The spectra are combined from NIR and mid-IR measurement results. The smoothed curves indicate that the port overfill is less than 0.001 for the entire spectrum except near the extreme ends. In fact, further measurements with the source blocked at the instrument indicate that the levels shown in Fig. 3 are most likely an overestimate. The source of this apparent offset is under investigation.

Another source of error belonging to the second category is the spatial and angular non-uniformity of the sphere throughput. The error from throughput non-
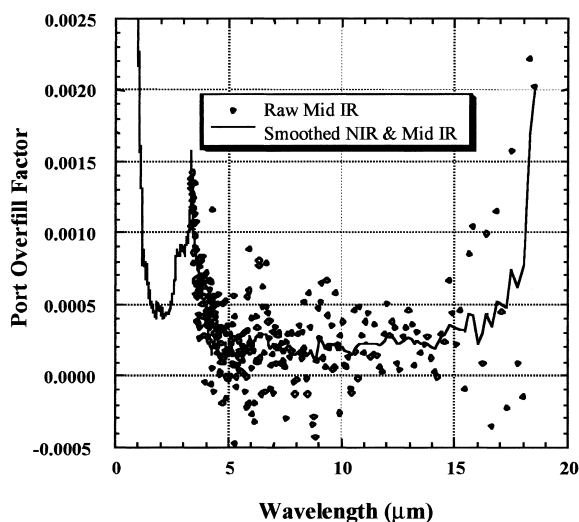

Fig. 3. Port overfill measurement result. Combined near infrared and mid-infrared spectra of the measured signal of the empty sample port illuminated in reflectance mode, ratioed to the standard sphere wall reference signal. Due to an unidentified offset signal, the contribution from actual scattered light may be less than that shown in this figure.

uniformity is significantly larger than from the minor sources of error mentioned above and provides the dominant contribution to the expanded measurement uncertainty. This would be true for any absolute method used. Characterization of this non-uniformity is discussed in Section 3.2 below.

3.2. Integrating sphere throughput mapping

The throughput of an integrating sphere is never perfectly uniform. There are several factors that lead to this result. Coatings are not perfect Lambertian diffusers (BRDF=constant). There is generally a variation in the BRDF with angle of incidence as well as with angle of reflection. The detectors used with spheres generally have a limited FOV and a responsivity dependent on incidence angle [13]. Baffles are generally required to overcome some of these problems, but cause problems of their own such as shadowing. All these factors lead to variations in the signal at the detector as a function of the direction leaving the sample of a given amount of flux: sphere throughput non-uniformity.

The evaluation of the sphere throughput uniformity is critical to an accurate determination of the measure-

ment uncertainties for diverse types of samples with varying scattering characteristics (BRDF). In addition, we can make use of the mapping measurement results to correct DHR measurement results if we know information about the BRDF of the samples. This is what we do to determine the absolute reflectance of the gold diffuser SRM samples, as is described in Section 4.

There are several possible approaches to mapping the uniformity of the sphere throughput. Ours is designed to:

1. minimize changes to the average sphere throughput as the beam is directed around the sphere;
2. avoid overfilling the sample port, especially at larger angles; and
3. map the sphere surface from the point of view of the sample (i.e. maintain a beam geometry as close as possible to that used in a reflectance measurement).

A set of 11 wedge mirror samples has been fabricated. Each mirror sample consists of an elliptical flat mirror (evaporated aluminum-coated glass) glued onto an aluminum cylinder of 38.1 mm average length×19 mm diameter which has the mirror end cut at an angle. On the other end, each cylinder has a centered tapped hole for mounting purposes and a reference flat used to enable alignment from one mirror sample to the next. The mirror samples form a set, with wedge angles ranging from $0°$ through to $45°$ in $5°$ increments, and an additional one at $22.5°$ (for examining the center great circle of the sphere).

For the mapping procedure, a motorized rotation stage is bolted to the sphere and the wedge mirror samples are inserted to position the center of the mirror surface at the center of the sample port. For the results described in this paper, an $8°$ compensating wedge was placed between the sphere mounting surface and the rotation stage. The purpose was to obtain alignment of the incident light along the center axis of the cylinders (and axis of rotation) and thereby eliminate variations in the angle of incidence and reflectance, as the sample was rotated. Also, this kept the cross-section of each sample, perpendicular to the beam, a constant through all rotations as well as between mirror samples. As shown in the top view of the sphere in Fig. 4, input light is reflected off the
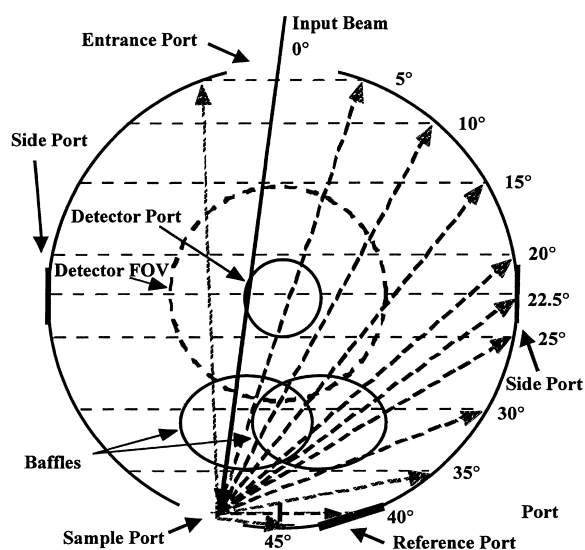

Fig. 4. Diagram showing the integrating sphere mapping coverage for the 11 wedge mirror samples used. These samples are positioned in the sample port tilted by an $8°$ compensating wedge plate that results in nominally normal incidence on the $0°$ wedge mirror sample and along the axis of rotation. Each sample has a different wedge angle: $0–45°$ in increments of $5°$, except for an additional wedge at $22.5°$. The dashed lines in the figure show the circles scanned by the reflected beams as the wedge samples are rotated about their central axis over $360°$.

mirror sample and directed to cover a circular cross-section of the sphere as the sample is rotated by the stage. The baffles are designed to prevent direct illumination of the detector port and its FOV. Hence the $22.5°$ mirror-sample-scan probes almost all the different regions of the sphere (as seen in Fig. 4) and should show the greatest range of throughput variation.

The sphere mapping procedure has been completely carried out at $10.6\,\mu m$ wavelength using a 4 W CO_2 laser system shown schematically in Fig. 5. The CO_2 laser is temperature-stabilized and the output beam is power-stabilized using an acousto-optic modulator and a room-temperature-stabilized MCT feedback detector. This system achieves a very good power stability (as measured by the sphere MCT detector) with drift of less than 0.2% over an hour time period. The polarizer and quarter-wave-plate are used to present circularly polarized light to the wedge mirror samples. As indicated in the figure, the sphere could also be rotated about its entrance port. This was used
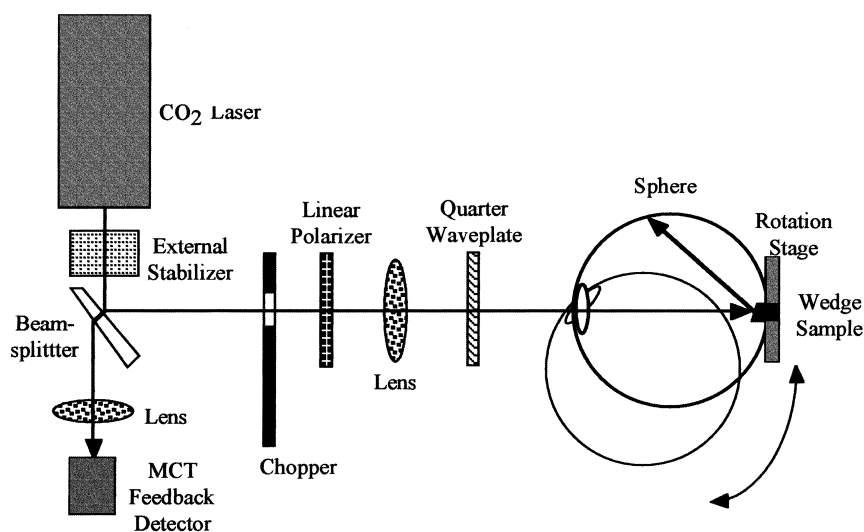
Fig. 5. Schematic of the integrating sphere mapping setup using a CO_2 laser source. The polarizer and quarter-wave-plate are used to effectively depolarize the light incident on the wedged mirror samples. One rotation stage is used to direct the reflected beam within the integrating sphere, and a second (not shown) is used to pivot the sphere about the entrance port for horizontal mapping and reference measurements. The external stabilizer uses a feedback signal from a (room) temperature-stabilized MCT detector, which monitors the CO_2 laser output via a wedged beam splitter.

to perform reference measurements and also to scan the sphere in a great circle orthogonal to the other mapping components. Not shown in the figure are attenuators that were placed in the beam path upstream of the beam splitter to reduce the power into the sphere to approximately 500 μW.

The mapping procedure was carried out for three configurations of the integrating sphere: (1) the 'clean' sphere without any baffles; (2) the sphere with diffuse baffles with a coating identical to that of the sphere wall; and (3) the sphere with specular gold-coated baffles. For each 360° rotation of the stage, 181 sample measurements were made in 2° increments, along with a number of reference measurements of a flat disk of the sphere wall material. The spot size on the sphere wall was ca. 4 mm in diameter. For spot sizes of ≤1 mm, speckle effects were observed.

A comparison of the three configurations for the sphere scanned with the 22.5° wedge mirror sample is shown in Fig. 6. As indicated in the figure, the scan cuts across the detector port or baffle, the detector FOV or baffle, and side port covers. To be noted is the dramatic improvement in the overall throughput uniformity with the addition of the baffles. The high throughput into the detector FOV without baffles

can be expected, and should roughly scale inversely with the size of the FOV [13]. It will also be noted that the throughput uniformity is better for the specular baffle configuration than for the diffuse baffle configuration. This is also to be expected because the reflectance of the specular baffles is near 0.99, whereas for the diffuse baffles, it is ∼0.90. The throughput structure near 190° in Fig. 6 in the 'no baffles' configuration represents the expected 10^{-3} leakage of the compound-hyperbolic-concentrator lens combination to the MCT detector [7]. Finally, one can observe dips in the throughput at the edges of the side port covers, where the fit is imperfect, as compared to small peaks in the throughput in the center of the covers, where the reflectance is 4% greater than that of the surrounding sphere wall. Analysis of this last observation led to the reevaluation of the method selected for the absolute reflectance determination.

The combined results of the complete set of wedge mirror samples are shown in Fig. 7. Only the configurations with baffles are shown. Several regions can be clearly identified: the baffles and the side ports. The bright spot in the lower left-hand corner of Fig. 7(a) is unfortunately the result of a specular reflection
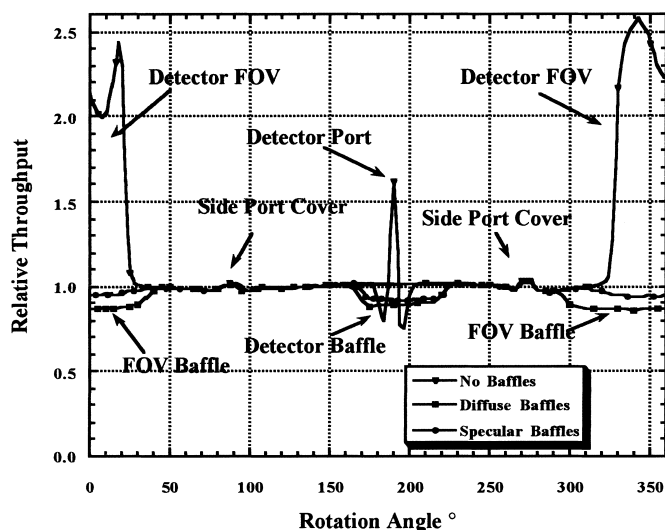
Fig. 6. Comparison plot of the spatial uniformity scan of the integrating sphere measured at 10.6 μm. Results are shown for three different arrangements of the sphere: (a) with no baffles, (b) with specular baffles, and (c) with diffuse baffles.
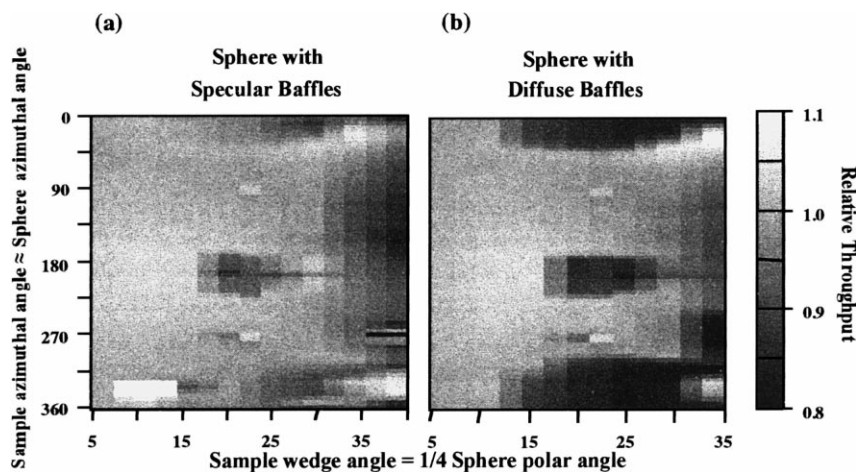

Fig. 7. Summary plot of the spatial uniformity mapping of the integrating sphere measured at 10.6 μm. Results are shown for two different arrangements of the sphere: (a) with specular baffles, and (b) with diffuse baffles. The coverage of the sphere is complete except for the positions corresponding to the top and bottom of the sphere (as viewed in Fig. 4). The scale is shown by the bar on the far right.

directly into the detector port (where the relative throughput rises to ∼2.0). Except for the reflection into the detector port, the specular baffle configuration clearly has more uniform throughput than the diffuse case. However, due to the large spike for the specular baffle case, we have chosen to keep the diffuse baffles installed until an appropriate redesign of the baffle locations can be performed. The span of the relative throughput variation is almost 0.3, which can repre-

sent the absolute worst case measurement scenario. In fact, as we shall see, the range expands further with decreasing wavelength. Another important observation is the symmetry of the results in Fig. 7 and the relatively constant and uniform throughput for the 'specular' and 'reference' regions of the sphere wall identified in Fig. 2.

The next step is to map the sphere throughput as a function of the complete spectral range of interest
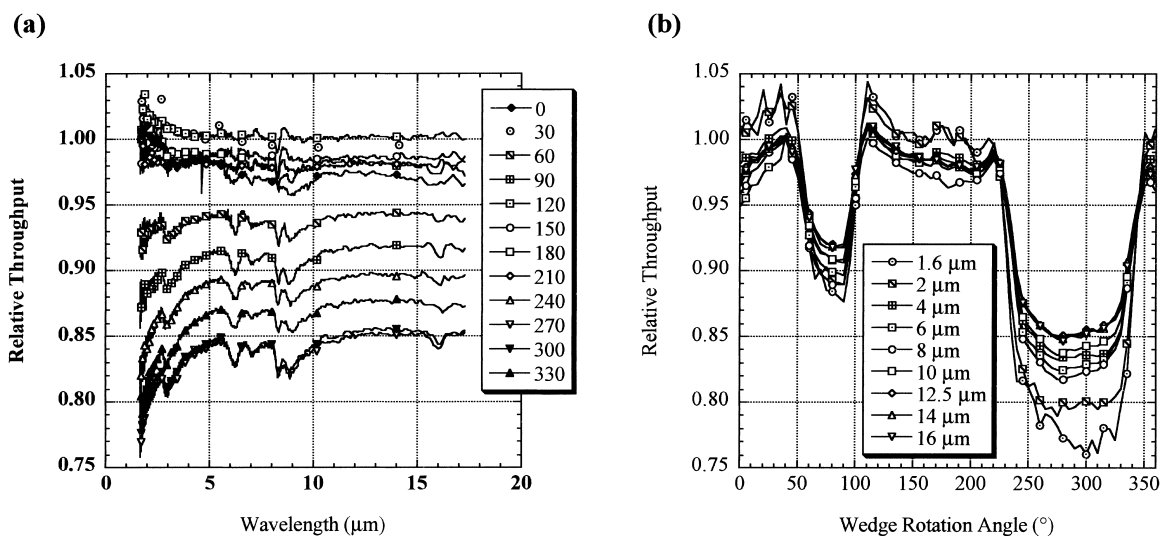
(a)

(b)

Fig. 8. Relative throughput spectra are shown in (a) for light reflected off the 22.5° wedge mirror samples rotated over 360° in 30° increments. The sphere is configured with diffuse baffles. Note that the absorption structure at various wavelengths due to the contaminant roughly scales with the overall level. The origin of the level variation between the curves in (a) can be seen more clearly in (b) as the reflected beam is scanned over the baffle positions. Only a sampling of the data at 30° is shown to remove the effects of noise due to water vapor absorption at the beginning of the measurement.

using the FT input beam. The FTIR-to-sphere interface optics layout is detailed in Fig. 1 of [9]. The initial results are shown in the next two figures. In Fig. 8(a), relative throughput spectra are shown for the 22.5° wedge mirror sample rotated over 360° in 30° increments. Data were taken at 5° angular increments. Note that the absorption structure at various wavelengths, primarily due to remnants of the sphere-coating process and adsorbed water (referred to hereafter as 'contaminant') [14], roughly scales with the overall level. The origin of the level variation between the curves in Fig. 8(a) can be seen more clearly in Fig. 8(b) which shows the throughput variation as a direct function of angle at selected wavelengths. As in the CO_2 laser case, the throughput is significantly reduced in the baffle regions of the scan (centered on rotation angles of 80° and 290°). Structure in the curves in the regions of the side port covers (near 10° and 190°), is less clear than in the CO_2 laser case in Fig. 6, because of the larger spot size (2.5 cm diameter) of the FTIR beam. The increasing non-uniformity of throughput at shorter wavelengths is to be expected if one considers the decreasing reflectance of gold at the shorter wavelengths and the strong dependency of sphere throughput on the average wall

reflectance. These results are a demonstration of the effects of wall reflectance on throughput uniformity and must be considered in any sphere design [6].

The combined results for all wave numbers (wavelengths) for the 22.5° wedge mirror sample scan are shown in Fig. 9. Additional measurements taken over the NIR up to 310° are also included in the map. A wave number scale is used because the FTIR data are generated in constant wave number interval. This tends to emphasize the NIR in the figure. The structure at ~1600 cm^{-1} is due to unstable purge conditions at the beginning of the measurement series. Also the noisy behavior at the largest wave numbers in going from one angle to the next is related to a temporary problem with short-term FTIR drift (up to 2%, as compared to 0.1% normal) and is not inherent to the sphere performance. The scale is shown at the bottom of the figure. The trend to greater non-uniformity with increasing wave number can be clearly seen.

The spectral sphere throughput mapping will be completed in the near future. The wedge mirror samples have been re-coated with sputtered gold for better performance [9]. For the present, most measurements on diffuse samples are made with the integrating sphere in the diffuse baffle configuration. This is to
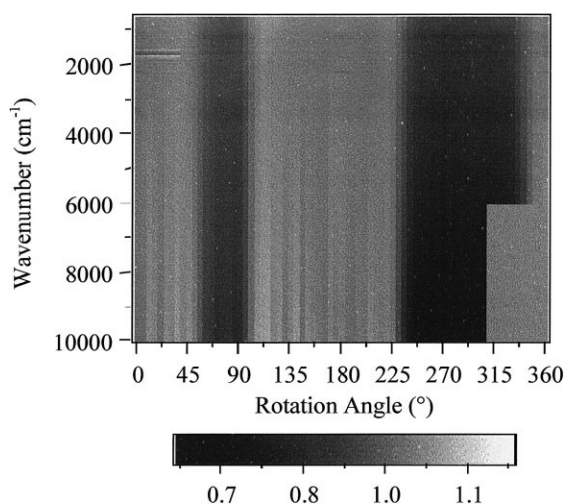
Fig. 9. Spectral sphere uniformity map for central vertical cross-section from 22.5° wedge sample scan. The data represent combined near infrared and mid-infrared spectral scans from 560 through to 10 000 cm^{-1}, and wedge scan angles in 5° increments from 0° through to 360°. Three discernable artifacts not associated with the sphere uniformity are: (a) structure due to atmospheric water vapor at ~1600 cm^{-1} at the top left, (b) a block of missing data above 6000 cm^{-1} at the bottom right, and (c) a slightly noisy behavior at the largest wave numbers in going from one angle to the next due to short term drift of the FT instrument. The other features, discussed further in the text are real and associated with the integrating sphere behavior.

avoid problems from the strong spike in the throughput in the specular baffle configuration. Hopefully, an appropriate readjustment of the baffle position and alignment in the sphere will allow the use of specular baffles and reduce the measurement error and the associated uncertainties. Raytracing results will be required to do this. The positioning should be governed by the same criteria used to position the diffuse baffles, with the additional consideration of the specular nature of the baffles. Namely, avoid any interchange of light between the sample, reference, and the detector and its FOV.

4. Method for determination of absolute directional-hemispherical reflectance

The method for the absolute DHR determination consists simply of performing the reflectance measurement as described in Section 2 and Fig. 2 to produce a DHR value $\rho_0 = V_s/V_r$, where V_s is the measured signal in the sample reflectance geometry

and V_r is the signal in the reference geometry. For a specular sample, the relative expanded uncertainty is approximately 0.3%. Small corrections to ρ_0 can be performed to reduce the uncertainty for those sources of error which have been characterized. For a sample known to be nearly Lambertian, the correction to ρ_0 is

$$\rho = \frac{\rho_0}{\tau_{avg}}, \tag{1}$$

where

$$\tau_{avg} = \frac{1}{2\pi} \int\limits_{0}^{2\pi} \int\limits_{0}^{\pi/2} \tau(\theta, \phi) \sin(\theta)\, d\theta\, d\phi \tag{2}$$

is the relative throughput (relative to the throughput for the specular direction) averaged over the sphere surface and (θ, ϕ) are the output angles of the reflected light leaving the sample. For a sample with arbitrary scattering character, we would use

$$\rho = \rho_0 \frac{(1 + 1/\tau_{avg})}{2}, \tag{3}$$

and cite a relative expanded uncertainty of approximately

$$U = \frac{(1/\tau_{avg} - 1)}{2}, \tag{4}$$

reasoning that most samples would have the reflected light encounter a sphere throughput somewhere in between the perfectly specular and perfectly diffuse case. This conclusion will be tested by calculating throughput corrections for samples with various types of scatter distributions; the uncertainty estimates will then be correspondingly adjusted.

For some samples, such as the DHR standards under development, a reduction in the uncertainty of the DHR values can be achieved by directly measuring the sample's scattering character, i.e. by measuring its bi-directional reflectance distribution function (BRDF) under the sphere measurement condition of 8° incidence, $f(8°; \theta, \phi)$. The average relative throughput, τ_{avg}, can be calculated from

$$\tau_{avg} = \frac{1}{\rho_{0calc}} \int\limits_{0}^{2\pi} \int\limits_{0}^{\pi/2} f(8°; \theta, \phi) \cos(\theta) \tau(\theta, \phi) \sin(\theta)\, d\theta\, d\phi, \tag{5}$$

where

$$\rho_{0calc} = \int\limits_{0}^{2\pi} \int\limits_{0}^{\pi/2} f(8°; \theta, \phi) \cos(\theta) \sin(\theta) \, d\theta \, d\phi.$$

Then the absolute DHR is given by

$$\rho = \frac{V_s}{V_r} \left[\frac{\int_0^{2\pi} \int_0^{\pi/2} f(8°; \theta, \phi) \sin(2\theta) \, d\theta \, d\phi}{\int_0^{2\pi} \int_0^{\pi/2} f(8°; \theta, \phi) \tau(\theta, \phi) \sin(2\theta) \, d\theta \, d\phi} \right]. \tag{6}$$

Note that if the throughput is perfectly uniform, the relative throughput $\tau(\theta, \phi) = 1$, and Eq. (6) reduces to $\rho = \rho_0$, so that corrections to the directly measured reflectance ratio are only to the extent of the throughput non-uniformity. Note also that there always is one non-uniform feature: the entrance port (or viewing port in a HDR device). For the sphere analyzed herein, for a Lambertian sample, the entrance port loss is ~1%.

5. Infrared diffuser, reflectance standard characterization

When the integrating sphere coating was selected, we decided to use the same material for the calibrated DHR standards. This material consists of an aluminum substrate coated with plasma sprayed copper and then over-coated with electroplated gold. The samples are produced by Labsphere [8] (also see footnote 1). As mentioned earlier, this material reasonably approaches a Lambertian scatterer. At the present time the standard samples are in hand, and we are beginning the characterization process.

Eq. (6) represents the primary method for the determination of the absolute DHR for standard samples. However, until the spectral sphere mapping process is completed, we are applying two additional techniques to obtain the DHR of the standard samples, which are described below.

The first method involves a scale transfer from the UV–Vis–NIR reflectance standard work at NIST, using pressed powder polytetrafluoroethylene (PTFE). A carefully pressed PTFE sample was measured on the integrating sphere system [15]. The simple result obtained from Eq. (1) was then ratioed to the available standard values for the pressed PTFE DHR [16]. The
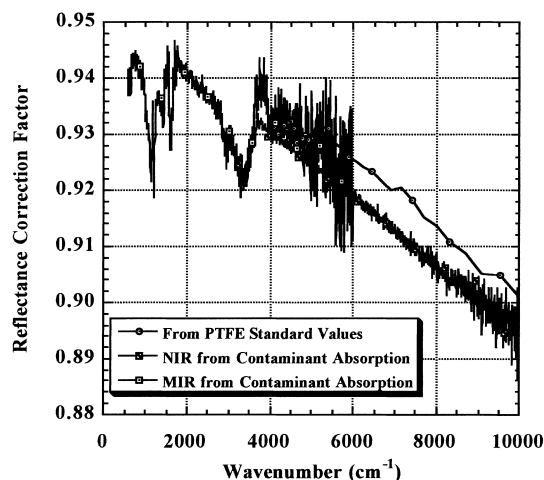

Fig. 10. Calibration curve comparison between PTFE and contaminant absorption peak methods. The PTFE method curve begins at 4000 cm^{-1}, and the NIR contaminant absorption peak method curve begins at 2900 cm^{-1}. For the contaminant peak method, the NIR calibration curve offset from the MIR curve can be attributed to the same temporary FTIR drift problem in the NIR which is in evidence in Fig. 9.

resulting calibration curve covers the spectral range 1–2.5 μm, where the UV–Vis–NIR and FTIR systems overlap. This curve is one of the three correction factor curves shown in Fig. 10. These calibration curves are used to obtain the absolute DHR reflectance of nearly Lambertian samples (by dividing into the directly measured reflectance value).

The second additional method is used to obtain the other two curves in Fig. 10. We noted earlier in Fig. 8(a) that the strength of the absorption structure in the spectra seemed to be correlated to the overall level. This relationship is shown in Fig. 11. The ratio of the relative throughput at 1130 cm^{-1} to the base level at 700 cm^{-1} is plotted against the base level for all 72 spectra obtained from the sphere mapping scan series. The linear least squares fit to the data is shown as well. The correlation is a reasonable one to expect. Since the local sphere wall reflectance has proven to be fairly uniform, the varying throughput for a reflected ray can be primarily associated with a greater number of reflections within the sphere before detection. Thus both the broadband absorption represented by the relative throughput level and the contaminant absorption structure should be equally affected by the directionality of the sample reflected light. For a
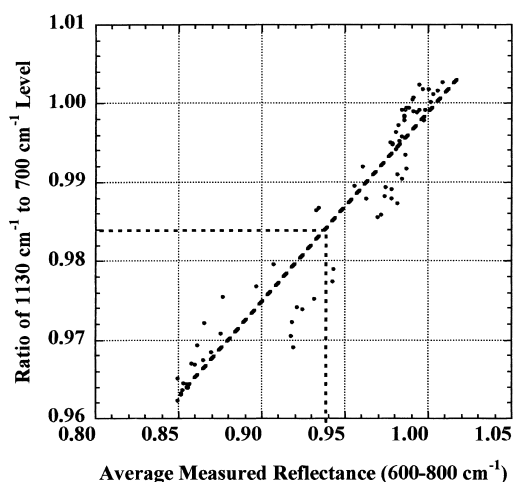
Fig. 11. Correlation of sphere throughput to level of contaminant absorption band strength. The measured levels at 1130 (contaminant absorption region) and 700 cm^{-1} (averaged over 600–800 cm^{-1}) are ratioed and plotted vs. the level at 700 cm^{-1} for all curves represented in Fig. 8. The linear least squares fit are shown as a dashed line. See text for description of light dashed lines.
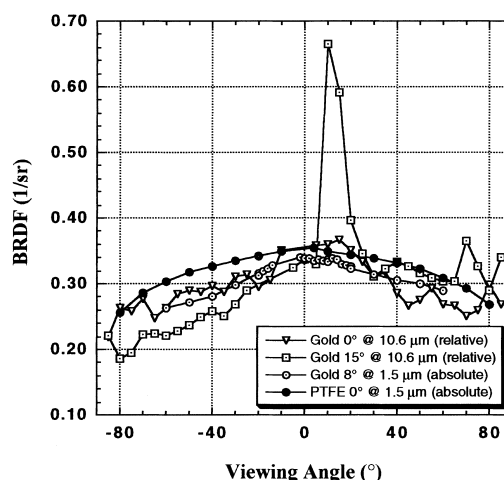

Fig. 12. BRDF of PTFE and gold diffuser SRM samples. Each curve represents an average of results using s- and p-polarized incident light. The BRDF of the PTFE and gold diffuser measured at 1.5 μm have very similar structure, with the gold diffuser having consistently slightly lower values. At 10.6 μm, the older gold diffuser sample BRDF has specular peaks at 15° and 0° (not directly observable for 0°) [4]. The remaining structure is also very similar to the measurement results shown for 1.5 μm.

specular sample, the relative throughput for sample and reference measurements is very close to 1, whereas for a scattering sample, the strength of the contaminant structure appearing in the raw reflectance spectra is an indication of how diffuse the character of the reflected light is.

In Fig. 12, the BRDF of PTFE and the infrared gold diffuser standard samples are compared at 1.5 μm. The measurements were performed using the UV–Vis–NIR STARR facility [17]. An examination of Fig. 12 reveals that the BRDF structure of the gold diffuser is very similar to that of the PTFE pressed powder. The primary difference is the slightly lower level of the gold diffuser. A similar but older version of the gold diffuser was measured at 10.6 μm wavelength and at 0° and 15° incidence [4]. It can be seen that except for the specular peak observed in the 15° results, the 8°–1.5 μm curve lies between the 0° and 15°–10.6 μm curves. This suggests that the BRDF of the gold diffuser is not only a reasonable approximation to a Lambertian diffuser, but also retains this character beyond 10 μm. The specular component of the 15° curve contains approx. 3% of the total reflectance. The error introduced by this in the determination of the sample DHR is insignificant. To determine whether the specular component increases to become

significant at longer wavelengths, normal incidence (specular component removed) measurements will be performed. The 10.6 μm measurements will soon be repeated on the new samples that may exhibit a reduction in the specular component. Note that the 10.6 μm results are relative BRDF.

Based on the BRDF results discussed above and additional measurement results that will be published in the future, including normal incidence measurements, we conclude that the gold diffuser sample is a good approximation to a Lambertian scatterer. It is used to obtain the reflectance correction factor in the mid-IR (MIR) for sphere measurements of diffuser samples, shown as two curves in Fig. 10. A direct measurement of the DHR of one of the gold diffuser SRM samples is shown in Fig. 13. The relative strength of the contaminant absorption line at 1130 cm^{-1} obtained from the DHR measurement (Fig. 13) is used to determine an absolute reflectance value near 700 cm^{-1} from Fig. 11 as described in the following. The horizontal dashed line in Fig. 11 indicates where the gold diffuser result lies along the correlation line. The corresponding (vertical dashed line) average measured reflectance value is approx.
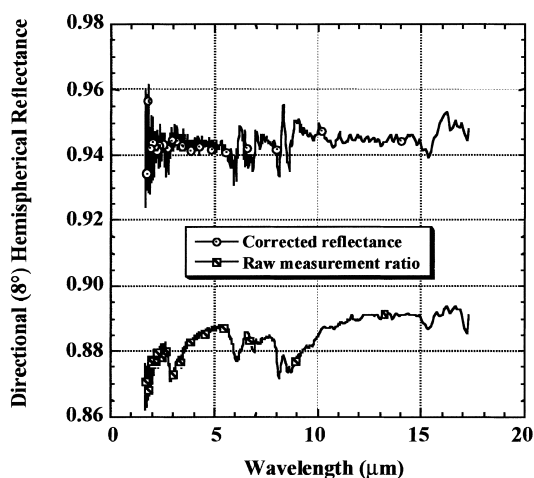
Fig. 13. Plot of directional hemispherical reflectance of gold diffuser SRM sample, before and after correction for throughput variation.

0.938. This number represents the expected result of a reflectance measurement (near 700 cm^{-1}) of a perfectly reflecting sample (i.e. ρ=1.0), with the same scattering characteristics as gold diffuser sample. This means that the direct measurement results of the gold diffuser shown in Fig. 13 should be corrected by dividing by 0.938 near 700 cm^{-1}. This value is used to select one of the curves from the complete set of curves represented by Fig. 8(a). The calibration curve for the MIR selected in this way, and shown in Fig. 10, is the 60° curve from Fig. 8(a).

To the extent that the gold diffuser is an ideal Lambertian scatterer, the 60° curve from Fig. 8(a) represents the 'average' throughput of the sphere and should roughly agree with the results calculated from Eq. (2) and closely match the results of Eq. (5) (to be obtained after the spectral mapping is completed). The other NIR curve shown in Fig. 10 is the 60° scan taken from the NIR mapping series. The offset between these two curves is associated with the FTIR NIR short-term drift problem (now corrected). Note the good agreement between the curves in Fig. 10 obtained from the two different calibration methods in the region of spectral overlap from 4000 to 6000 cm^{-1} (NIR PTFE and MIR contaminant method curves). Except for the level difference (due to the drift), the NIR PTFE and contaminant method curves also agree reasonably well.

A single calibration curve for diffuse sample DHR evaluation covering the spectral range 1–18 μm is obtained by combining the NIR PTFE and the MIR contaminant absorption calibration curves. In particular the DHR calibration curve is applied to the gold diffuser, reflectance standard sample DHR curve shown in Fig. 13 to obtain the absolute DHR. At the moment the estimated expanded uncertainty for the DHR calibration of the gold diffuser reflectance standards is ∼0.02. We anticipate a reduction in the uncertainty with the completion of the sphere mapping measurements.

6. Summary and conclusions

A facility for measurement of absolute directional-hemispherical reflectance in the infrared spectral range 1–18 μm has been established and a standard reference material (SRM) available for purchase is in the characterization phase. Several methods are available to perform refinement corrections to the raw reflectance data, which can reduce the uncertainty of the DHR values. A number of sources of measurement error can occur. However, characterization of these error sources can lead to their correction or elimination. The primary error source for diffuse sample measurement is the throughput non-uniformity (i.e. as a function of the direction angles of the light leaving the sample). This problem is dealt with by carefully mapping the structure of the non-uniformity. The resulting information is coupled with sample scattering measurement data to reduce uncertainties. Alternatively, the characterization provides the necessary knowledge required to accurately assess the measurement uncertainties. Finally, the mapping results can be used to improve the design of the next generation spheres.

References

[1] A. Migdall, G.P. Eppledauer, Proceedings of the NEWRAD 97 Conference, Tucson, AZ, 27–29 October 1997, Metrologia 35 No. 4, (1998), in press.

[2] A. Migdall, G.P. Eppledauer, NIST Special Publication 250-42 (1998).

[3] K.R. Lykke, P.S. Shaw, G.P. Eppledauer, L.M. Hanssen, Proceedings of the NEWRAD 97 Conference, Tucson, AZ, 27–29 October 1997, Metrologia 35, No. 4 (1998), in press.

[4] L.M. Hanssen, in: C. Burgess, D.G. Jones (Eds.), Spectro-photometry, Luminescence and Colour; Science and Compliance, Elsevier, Amsterdam, 1995, pp. 115–128.

[5] R.R. Willey, Appl. Spectrosc. 30 (1976) 593–601.

[6] L.M. Hanssen, Appl. Opt. 35 (1996) 3597.

[7] D.B. Chenault, K.A. Snail, L.M. Hanssen, Appl. Opt. 34 (1995) 7959.

[8] Labsphere Inc., PO Box 70, Shaker Street, North Sutton, NH 03260.

[9] S.G. Kaplan, L.M. Hanssen, Anal. Chim. Acta (1999).

[10] L.M. Hanssen, Appl. Opt. (1998), submitted.

[11] S.G. Kaplan, L.M. Hanssen, R.U. Datla, Appl. Opt. 36 (1997) 8896.

[12] Z.M. Zhang, C.J. Zhu, L.M. Hanssen, Appl. Spectrosc. 51 (1997) 576.

[13] L.M. Hanssen, Appl. Opt. 28 (1989) 2097.

[14] Art Springsteen, Lapsphere Inc., Personal Communication.

[15] P.Y. Barnes, J.J. Hsia, Natl. Inst. Stand. Technol. Technical Note (1995) 1413.

[16] V.R. Weidner, J.J. Hsia, J. Opt. Soc. Am. 71 (1981) 586.

[17] P.Y. Barnes, E.A. Early, A.C. Parr, Spectal Reflectance, Natl. Inst. Stand. Technol. (Special Publication) (1998) 248–250.